European Journal of Mechanics / A Solids 116 (2026) 105941

Contents lists available at ScienceDirect

European Journal of Mechanics / A Solids

journal homepage: www.elsevier.com/locate/ejmsol

Full Length Article

Enhanced super-harmonic resonance in piezoelectrically laminated curved microbeam resonators under fringing-field electrostatic actuation

Zahra Rashidi [a], Saber Azizi [b,*], Omid Rahmani [a]

[a] Smart Structures and New Advanced Materials Laboratory, Mechanical Engineering Department, University of Zanjan, Zanjan, Iran
[b] Faculty of Science and Engineering, Aerospace Engineering Department, Swansea, UK

ARTICLE INFO

Keywords:
Nonlinear dynamics
Super-harmonic secondary resonance
Low-frequency MEMS resonators
Wide-band
Initially curved microbeam
Fringing-field electrostatic actuation
Piezoelectric actuation

ABSTRACT

Achieving low-frequency MEMS resonators while maintaining the compact size of MEMS sensors has long been a challenge in MEMS design and fabrication. This study focuses on the super-harmonic resonance regions and associated bifurcation points of a curved microbeam sandwiched between two piezoelectric layers and subjected to fringing-field electrostatic actuation. The nonlinear equations of motion are derived, and the dependence of the electrostatic force on displacement is analysed using a finite element approach. The microbeam is excited by a combination of DC and AC electrostatic actuation, along with a tuning DC piezoelectric voltage. The influence of the piezoelectric voltage on the variation of the natural frequency under a given DC electrostatic excitation is examined. The frequency response curves are obtained over a broad excitation range, extending from below the primary resonance, through the super-harmonic regime, and beyond the primary resonance region. Bifurcation points are identified using Floquet multipliers. The results indicate that strong quadratic and cubic nonlinearities lead to the emergence of super-harmonic resonance zones of orders 1/2 and 1/3 in the frequency response, enabling the development of low-frequency resonators while retaining the advantages of MEMS-scale sensors. This effect is particularly significant in the design of MEMS energy harvesters, facilitating energy extraction from low-frequency mechanical noise. The simultaneous presence of nonlinearities of orders 1/2 and 1/3 and even higher orders generates multiple resonance zones within the super-harmonic regime, enabling the design of broadband low-frequency energy harvesters and MEMS wide-bandpass filters.

1. Introduction

Microelectromechanical systems (MEMS) have been exploited for various applications due to their many advantages, including easy fabrication, low power consumption, low cost, and high accuracy and efficiency. Applications of microelectromechanical systems include resonators, various types of sensors and actuators, switches, non-volatile mechanical memories, and band-pass filters (Mestrom et al., 2008; Bogue, 2013; Bell et al., 2005; Rebeiz and Muldavin, 2001; Shim et al., 2012). Electrostatically actuated resonant microbeams constitute the main structures of MEMS. In these structures, the microbeam is excited by a combination of dc and ac voltages. There are various methods for exciting microelectromechanical systems at resonances. The excitation frequency can be set near the natural frequency, in other words, the system is under primary resonant excitation (Younis and Nayfeh, 2003; Kacem et al., 2011; Bouchaala et al.; Caruntu and Luo, 2014; Ghayesh et al., 2013/10; Ruzziconi et al., 2013; Tajaddodianfar et al., 2017). In this regard, Younis and Nayfeh (2003) investigated the nonlinear response of a resonant straight microbeam under parallel-plate electrostatic actuation. By adopting the multiple time-scales perturbation method, they presented frequency response curves in the vicinity of the primary resonance and showed that the DC electrostatic load affects the quantitative and qualitative nature of the frequency response curves. In another study, Kacem et al. (2011) evaluated the nonlinear vibrations of MEMS resonant sensors around the primary resonance. The solution method is based on the Galerkin decomposition method and the averaging method. They reported changes in the sensitivity of the resonant sensor to electrostatic loading. In addition to primary resonance, microelectromechanical systems may be subject to secondary resonance excitation of super-harmonic and sub-harmonic types due to their nonlinear nature (Nayfeh and Younis, 2005; Younesian et al., 2014; Najar et al., 2010; Azizi et al., 2016; Eihab and Ali, 2003). Nayfeh and Younis (2005) studied the nonlinear dynamics of MEMS resonators under sub-harmonic and super-harmonic excitations. They showed the

* Corresponding author.
E-mail address: saber.azizi@swansea.ac.uk (S. Azizi).

https://doi.org/10.1016/j.euromechsol.2025.105941
Received 21 April 2025; Received in revised form 28 October 2025; Accepted 31 October 2025
Available online 5 November 2025

effect of various parameters, including DC voltage, damping, and AC excitation amplitude, on the frequency response curve in the vicinity of super-harmonic resonance. Esmailzadeh et al. (Younesian et al., 2014) analysed the primary and secondary resonances of double-clamped microbeams. They considered higher-order nonlinear terms in the equation of motion and studied all resonant states using the multiple time-scales perturbation method. Parametric resonance and internal resonance are other resonances that may be activated in a micro-electromechanical system under certain conditions (Caruntu and Martinez, 2014; Ruzziconi et al., 2021).

In recent years, initially curved microbeams have gained a special place in MEMS due to their rich and unique nonlinear dynamic behavior. Bistability, snap-through motion, large amplitude displacements, and high sensitivity are among the advantages of initially curved microbeams (Rashidi et al., 2024). The phenomena present in arch microbeams are used in a wide variety of MEMS applications such as actuators, sensors (Najar et al., 2020), band-pass filters (Ouakad, 2013), non-volatile mechanical memories (Charlot et al., 2008), and in many other applications such as switches (Younis et al., 2010) that require two distinct stable states. The snap-through phenomenon in micro-electromechanical switches enables switching without adhesion of the structure to the substrate, which significantly limits the performance of pull-in-based switches. Due to such advantages and applications, studying the resonant behavior of these structures is of great interest (Najar et al., 2020; Younis et al., 2010; Ouakad and Younis, 2010; Ramini et al., 2016; Ghayesh and Farokhi, 2017; Tajaddodianfar et al., 2015; Ghayesh et al., 2015; Nikpourian et al., 2019a). Ouakad and Younis (2010) investigated the dynamic behavior of MEMS arch resonators in the vicinity of the primary resonance. They used the multiple time-scales perturbation method to obtain the forced vibration response of the arch. The results show locally a softening type behavior for the resonant frequency for all DC and AC loadings as well as the initial elevation of the arch. Theoretical and experimental investigation of the nonlinear dynamic behavior of MEMS arches under electrostatic actuation is another research that has been conducted by Ramini et al. (2016). They showed that when the excitation is close to the first resonant frequency, softening behavior is observed due to the quadratic nonlinear effect caused by the arch geometry and the electrostatic force. Limited studies have addressed the nonlinear dynamics of initially curved microbeams in the vicinity of secondary resonance (Younis et al., 2010; Nikpourian et al., 2019a). Younis et al. (2010) investigated the secondary resonance of MEMS arches under electrostatic excitation. The results have shown a variety of interesting nonlinear phenomena such as hysteresis, softening behavior, dynamic snap-through, and dynamic pull-in. The results also demonstrate the potential for using MEMS arches as band-pass filters and low-power switches. One of the most important concerns regarding parallel-plate electrostatic actuation is the pull-in instability, which results in adhesion leading to collapse of the device. Unlike parallel-plate electrostatic actuation, where the electrode is placed below the microbeam, in the fringing-field electrostatic actuation arrangement (Michel et al., 2004) the electrodes are placed on either side of the microbeam. In such an excitation method, due to the non-contact operation, the pull-in instabilities are avoided and the large-amplitudes are not limited by pull-in instabilities and squeeze film damping. Therefore, this actuation arrangement leads to an increase in the life of the device with a large displacement. Very limited research has investigated the resonant behavior of initially curved microbeams under fringing-field electrostatic actuation (Rashidi et al., 2023a, 2024; Tausiff et al., 2019). Tausiff et al. (2019) investigated the primary resonance of MEMS arches under the fringing-field electrostatic actuation using the multiple time-scales method. Since the multiple time-scales method has been used, their results are only valid for small deformations. Rashidi et al. (2024) studied the chaotic dynamics of curved microbeam resonators under simultaneous piezoelectric and fringing-field electrostatic actuation. However, a review of previous studies shows that the secondary resonance analysis of this structure has not been performed so far.

To harvest maximum energy from ambient vibration, the resonant frequency of the energy harvester must match the frequency of the ambient vibration. Any deviation between these two frequencies will cause a significant reduction in the harvested power (Jaber et al., 2016; Liu et al., 2011; Williams and Yates, 1996). In fact, the frequencies of environmental vibration sources are relatively low (Liu et al., 2011; Roundy et al., 2003), while the resonant frequencies in the MEMS are large (on the order of kHz) due to the small size of the MEMS structure. As a result, designing a low frequency MEMS resonator for energy harvesting applications is both critical and challenging. Also, the wide band operating frequency range of the resonator is crucial for high efficiency of energy harvesters and band-pass filters. Liu et al. (2011) proposed a piezoelectric energy harvester that can achieve a low resonant frequency and also has a wide band operating frequency range. Nisanth et al. (2021) designed and optimized a low frequency MEMS piezoelectric energy harvester. They investigated the effects of geometric parameters on the device performance and optimized these parameters to achieve a lower resonant frequency and higher output power. Also, in references (Nguyen et al., 2010; Pasharavesh and Ahmadian, 2017; Han et al., 2014; Miller et al., 2011; Gu, 2011), various strategies for designing low frequency wide band MEMS resonators have been presented.

In this paper, the super-harmonic secondary resonance of an initially curved microbeam under simultaneous piezoelectric and fringing-field electrostatic actuation is comprehensively investigated. Piezoelectric actuation is used to adjust the resonant frequency and control the dynamic behavior of the system. The governing equation of motion, including nonlinearities due to mid-plane stretching, initial curvature, and fringing-field electrostatic actuation, is presented and discretized into a reduced-order model using the Galerkin method. The frequency response curves near the super-harmonic resonance are obtained by a combination of shooting (Nayfeh and Balachandran, 2008; Younis, 2011) and continuation (Dhooge et al., 2003) methods. The focus of the study has been on the lower frequency resonance regions which are important particularly in the design of energy harvesters and low frequency band pass filters. The existence of various orders of nonlinearity (mainly quadratic and cubic) has enabled the appearance of super-harmonic resonance regions of orders 1/2 and 1/3 and in some cases their collision which ends up with wide-band-low-frequency resonance zones. Bifurcation analysis has been carried out and the types of the bifurcation points are determined based on the loci of the Floquet multipliers with respect to the unit circle on the complex plane. It has been illustrated that the studied model, which incorporates two lateral electrodes, can undergo large deflections without triggering pull-in instability. This behaviour highlights the effect of nonlinear terms and, consequently, enables the emergence of low-frequency resonance zones.

2. Problem formulation

The schematic of a double-clamped initially curved microbeam is shown in Fig. 1. L, a and h are the length, width and thickness of the initially curved microbeam, respectively. w_0 denotes the initial curvature of the microbeam and is introduced by the function $w_0(x) = b_0(1 - cos(2\pi x/L))/2$, where b_0 is the initial rise of the midpoint of the microbeam. The microbeam is made of Silicon with E_b, υ_b and ρ_b as the Young's modulus, Poisson's ratio and density respectively. Since $a > 5h$, the effective modulus of elasticity is expressed as $\widetilde{E}_b = E_b/(1-\upsilon_b{}^2)$, where for convenience, the sign of $\sim$ on the effective modulus of elasticity is omitted. The initially curved microbeam is subjected to simultaneous piezoelectric and fringing-field electrostatic actuation. Two thin PZT layers with thickness h_p are deposited on the upper and lower surfaces of the microbeam. E_p, υ_p and ρ_p are the Young's modulus, Poisson's ratio, and density of the piezoelectric layers, respectively. Moreover, for electrostatic actuation, two fixed electrodes are

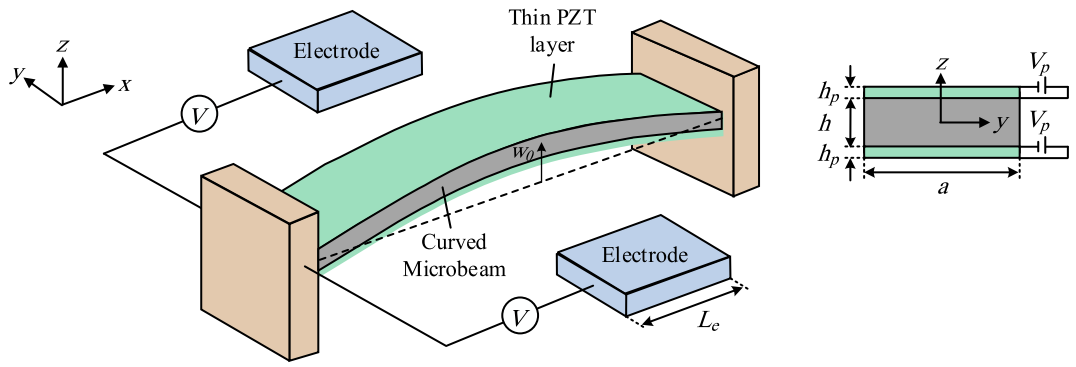

Fig. 1. Schematic of an initially curved microbeam resonator under piezoelectric and fringing-field electrostatic actuation.

symmetrically placed on both sides of the microbeam. The fixed electrodes are of length L_e and their width and thickness are the same as the width and thickness of the microbeam. The gap between the edge of the microbeam and each electrode is denoted by g.

For piezoelectric actuation, a dc voltage V_p is applied to the PZT layers. The resultant axial force applied to the microbeam in the longitudinal direction and is obtained as (Rashidi et al., 2023b)

$$F_p = -2e_{31}V_p a \tag{1}$$

where e_{31} shows the piezoelectric voltage constant. Moreover, by applying a potential difference V between the fixed electrodes and the microbeam, the transverse electrostatic force resulting from the electric fringing-fields is applied to the microbeam in the direction of the z-axis. The dependence of this fringing-field electrostatic force per unit length on the beam's transverse displacement was evaluated using finite-element simulations in COMSOL. A mesh-refinement convergence analysis was carried out to ensure the accuracy and stability of the computed forces, and the resulting data were then used to derive the force expression employed in the present model (Rashidi et al., 2023b)

$$f_e = -\frac{rsinh(q(w_0+w))\times V^2}{cosh^s(q(w_0+w))}H\left(x-\frac{L-L_e}{2}\right)H\left(L_e+\frac{L-L_e}{2}-x\right) \tag{2}$$

where r, q and s are the fitting parameters. The applied voltage is a combination of dc and ac voltages as $V=[V_{DC}+V_{AC}\,cos(\Omega t)]$. Also, $H(x)$ is the Heaviside step function.

Assuming the Euler-Bernoulli theory for a shallow microbeam and using Hamilton's principle, the nonlinear transverse vibration equation governing the system can be derived as (Rashidi et al., 2023b)

$$(EI)_{eq}\frac{\partial^4 w}{\partial x^4}+(\rho A)_{eq}\frac{\partial^2 w}{\partial t^2}+C_d\frac{\partial w}{\partial t}=\left[F_p+\frac{(EA)_{eq}}{2L}\int_0^L\left(\left(\frac{\partial w}{\partial x}\right)^2+2\frac{\partial w}{\partial x}\frac{dw_0}{dx}\right)dx\right]\left[\frac{\partial^2 w}{\partial x^2}+\frac{d^2 w_0}{dx^2}\right]+f_e \tag{3}$$

where

$$(EI)_{eq}=E_bI_b+E_pI_p=E_b\frac{ah^3}{12}+E_pa\left(h_ph\left(\frac{h}{2}+h_p\right)+\frac{2{h_p}^3}{3}\right)\quad(\rho A)_{eq}=\rho_bA_b+\rho_pA_p=\rho_bah+2\rho_pah_p\quad(EA)_{eq}=E_bA_b+E_pA_p=E_bah+2E_pah_p \tag{4}$$

In Eq. (3), C_d is the viscous damping coefficient. Also, the associated boundary conditions are given as

$$w(0,t)=0, w(L,t)=0, \frac{\partial w(0,t)}{\partial x}=0, \frac{\partial w(L,t)}{\partial x}=0 \tag{5}$$

To write the equation of motion and the corresponding boundary conditions in non-dimensional form, the dimensionless parameters are considered as follows

$$\widehat{w}=\frac{w}{h}, \widehat{w}_0=\frac{w_0}{h}, \widehat{x}=\frac{x}{L}, \widehat{L}_e=\frac{L_e}{L}, \widehat{t}=\frac{t}{\widetilde{t}}, \widetilde{\Omega}=\Omega\widetilde{t} \tag{6}$$

where, $\widetilde{t}=\sqrt{(\rho A)_{eq}L^4/(EI)_{eq}}$. Accordingly, the dimensionless equation of motion is obtained as

$$\frac{\partial^4 w}{\partial x^4}+\frac{\partial^2 w}{\partial t^2}+C\frac{\partial w}{\partial t}=\left[P+\alpha_1\int_0^1\left(\left(\frac{\partial w}{\partial x}\right)^2+2\frac{\partial w}{\partial x}\frac{dw_0}{dx}\right)dx\right]\left[\frac{\partial^2 w}{\partial x^2}+\frac{d^2 w_0}{dx^2}\right]-\alpha_2\frac{sinh(q(w_0+w))}{cosh^s(q(w_0+w))}H\left(x-\frac{1-L_e}{2}\right)H\left(L_e+\frac{1-L_e}{2}-x\right) \tag{7}$$

For simplicity, the over hat () has been omitted. Also, the non-dimensional parameters are

$$C=\frac{C_dL^4}{\widetilde{t}(EI)_{eq}}, P=\frac{F_pL^2}{(EI)_{eq}}, \alpha_1=\frac{h^2(EA)_{eq}}{2(EI)_{eq}}, \alpha_2=\frac{rL^4V^2}{(EI)_{eq}h} \tag{8}$$

In Eq. (8), the dimensionless parameter C is taken as $C=2\xi\omega$, where ξ

and ω are the damping ratio and natural frequency, respectively. The associated dimensionless boundary conditions are also obtained as

$$w(0,t)=0, w(1,t)=0, \frac{\partial w(0,t)}{\partial x}=0, \frac{\partial w(1,t)}{\partial x}=0 \tag{9}$$

The reduced order model (ROM) can be derived using the Galerkin decomposition method. Accordingly, the deflection of the microbeam is considered as follows

$$w(x,t)=\sum_{i=1}^{M} u_i(t)\varphi_i(x) \tag{10}$$

In Eq. (10), $\varphi_i(x)$ and $u_i(t)$ are the normalized mode shapes (Appendix A) and unknown generalized coordinates, respectively. By substituting Eq. (10) into Eq. (7), multiplying both sides of the equation by $\varphi_i(x)$, and integrating over the interval $x = [0, 1]$, the order reduction model is given as

$$\begin{aligned}
&\ddot{u}_n + C\dot{u}_n + \sum_{i=1}^{M} u_i(t)\int_0^1 {\varphi_i}^{(iv)}\varphi_n dx - P\left(\sum_{i=1}^{M} u_i(t)\int_0^1 {\varphi_i}''\varphi_n dx + \int_0^1 {w_0}''\varphi_n dx\right)\\
&-\alpha_1\left(\begin{array}{l}\displaystyle\sum_{i=1}^{M}\sum_{j=1}^{M}\sum_{k=1}^{M} u_i u_j u_k \int_0^1 \varphi_i'\varphi_j' dx \int_0^1 {\varphi_k}''\varphi_n dx + \sum_{i=1}^{M}\sum_{j=1}^{M} u_i u_j \int_0^1 \varphi_i'\varphi_j' dx \int_0^1 {w_0}''\varphi_n dx\\ \quad\displaystyle +2\sum_{i=1}^{M}\sum_{j=1}^{M} u_i u_j \int_0^1 \varphi_i' w_0' dx \int_0^1 {\varphi_j}''\varphi_n dx + 2\sum_{i=1}^{M} u_i \int_0^1 \varphi_i' w_0' dx \int_0^1 {w_0}''\varphi_n dx\end{array}\right)\\
&= -\alpha_2 \int_0^1 \frac{sinh\left(q\left(w_0+\sum_{i=1}^{M} u_i\varphi_i\right)\right)\varphi_n(x)}{cosh^s\left(q\left(w_0+\sum_{i=1}^{M} u_i\varphi_i\right)\right)} H\left(x-\frac{1-L_e}{2}\right)H\left(L_e+\frac{1-L_e}{2}-x\right)dx
\end{aligned} \tag{11}$$

where $n = 1, 2, 3, \ldots, M$.

The nonlinear equations of motion have been numerically integrated over time using the fourth-order Runge-Kutta (RK4) method to capture the time response in a given time. To analyse the steady-state periodic response, the frequency response curves were obtained using a combination of the shooting method and a continuation technique (Appendix B).

3. Results and discussion

The mechanical and geometrical properties of the studied model are given in Table 1.

The fitting parameters associated with the electrostatic force, determined by minimizing the least squares error, are presented in Table 2.

Table 1
Geometrical and material properties of the studied model.

Parameter	Symbol	Value (unit)
Microbeam length	L	800 (μm)
Microbeam width	a	12 (μm)
Microbeam thickness	h	2 (μm)
Initial elevation of the midpoint	b_0	4 (μm)
Microbeam density	ρ_b	2320 (Kg/m^3)
Microbeam Young's modulus	E_b	160 (Gpa)
Microbeam Poisson's ratio	υ_b	0.22
Length of the electrodes	L_e	0.3L
Distance to electrode	g	2 (μm)
PZT layer thickness	h_p	0.01 (μm)
PZT layer density	ρ_p	7500 (Kg/m^3)
PZT layer Young's modulus	E_p	76.6 (Gpa)
PZT layer Poisson's ratio	υ_p	0.3
Piezoelectric voltage constant	e_{31}	-9.29 $(Coulomb/m^2)$

Table 2
Fitting parameters of the electrostatic force.

Fitting parameters	r	q	s
Value	2.65×10^{-6}	0.97	1.33

To validate the results obtained using the Shooting method (Nikpourian et al., 2019a, 2019b), we compared them with those derived from the Matcont Toolbox MATLAB. As shown in Table 3, the comparison demonstrates a strong agreement between the two results.

Fig. 2 illustrates the effect of the variation of V_{DC} on the dimensional fundamental natural frequency of the microbeam. The results have been shown for three different piezoelectric voltages with different polarities.

As illustrated, the effect of applied V_{DC} depends on the region we are in, leading to either softening or hardening. As V_{DC} increases from zero, the natural frequency decreases, which implies that its effect on the natural frequency is softening. This behavior continues up to a critical voltage at which the system undergoes the most electrostatic softening, resulting in the lowest natural frequency. This point depends on the polarity of the piezoelectric voltage, and for positive polarity, it reaches its greatest value. This is because the positive polarity of the piezoelectric voltage imposes a tensile axial force on the beam, which increases the bending stiffness and, consequently, the natural frequency. Once this point is surpassed, the electrostatic excitation shifts to have a hardening effect on the natural frequency.

Fig. 3 illustrates the wideband frequency response curve, starting from well below the natural frequency (0), passing through the natural frequency (85.78), and continuing up to (220).

We have divided the frequency domain into three distinct zones (1, 2, and 3). Zone 1 is associated with the super-harmonic region, where

Table 3
Comparison between the Shooting vs. Matcont for $V_p = 0$V, $V_{DC} = 120$V, $V_{AC} = 30$V, $\xi = 0.06$

Ω	w_{max}(μm) Shooting Method	w_{max}(μm) Matcont
5	3.5556	3.5551
8	3.6239	3.6230
11	3.7795	3.7794
14	3.9231	3.9225
17	4.2558	4.2554
20	4.2654	4.2652
23	4.8166	4.8149
26	4.5184	4.5180
29	4.3664	4.3663
32	4.4382	4.4379
35	4.6525	4.6522

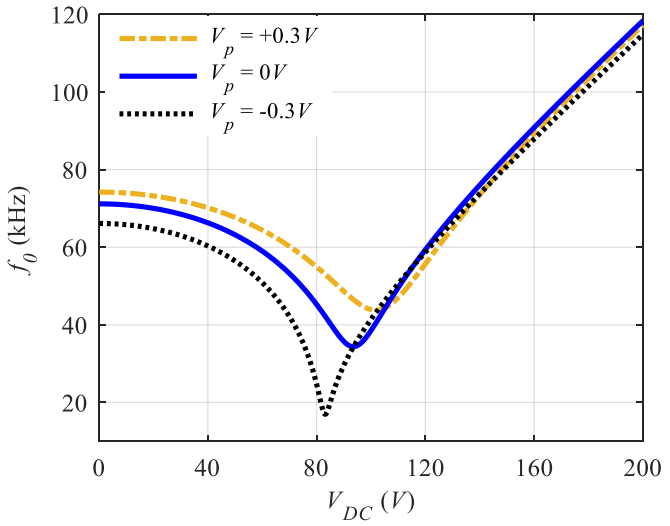

Fig. 2. Variation of the dimensional fundamental natural frequency versus the electrostatic voltage.

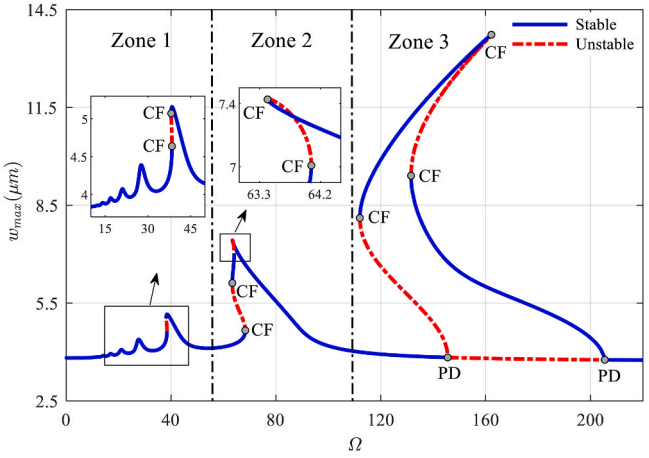

Fig. 3. Frequency response curve for $V_p = 0$V, $V_{DC} = 180$V, $V_{AC} = 60$V, $\xi = 0.06$

the excitation frequency is well below the primary resonance. This zone is significant because it allows for resonance at a fraction of the primary resonance, below the natural frequency. Zone 2 represents the primary resonance zone, while Zone 3 corresponds to the sub-harmonic resonance region, where resonance occurs at a multiple of the primary resonance. In Zone 3, although the resonance is secondary, the amplitude magnification is notably higher than at primary resonance, leading to a significant signal-to-noise ratio.

The types of bifurcation points are determined based on the loci of the Floquet multipliers with respect to the unit circle on the complex plane and illustrated in Fig. 3. Stable periodic orbits are represented by solid lines, while dashed lines indicate unstable periodic solutions. The label 'CF' denotes a cyclic fold bifurcation, where the Floquet multipliers exit the unit circle through +1. At the cyclic fold bifurcation, the stable and unstable manifolds approach each other as the bifurcation parameter (Ω) varies. When these manifolds intersect, they annihilate each other, and both solutions cease to exist beyond the bifurcation point. The label 'PD' stands for period doubling bifurcation which is normally associated with the sub-harmonic resonance of order 2. One of the advantages of this bifurcation is the improved signal-to-noise ratio, which has been a key point of interest in previous studies. At the period doubling bifurcation, the Floquet multipliers exit the unit circle through −1. When a period doubling bifurcation occurs, the stable periodic

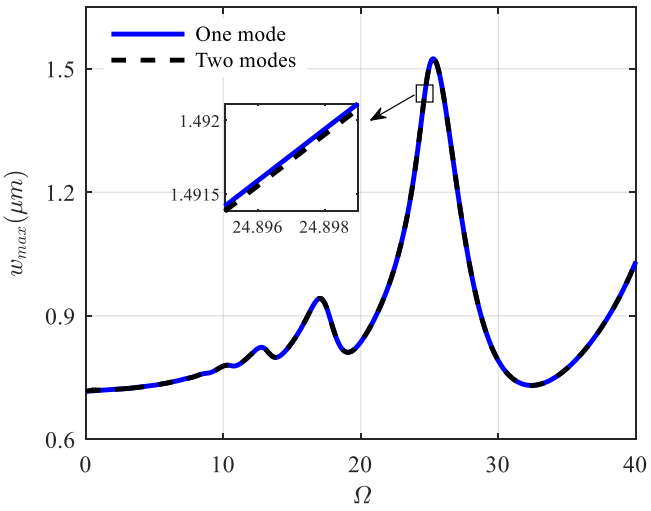

Fig. 4. Frequency response curve near super-harmonic resonance for $V_p = 0$V, $V_{DC} = 40$V, $V_{AC} = 30$V, $\xi = 0.06$

solution branch becomes an unstable periodic solution branch, and new periodic solutions with a period twice the period before the bifurcation point are born. In the remainder of this study, we focus on the response in Zone 1, as reducing the resonance frequency of MEMS structures particularly for low-frequency energy harvesters and band-pass filters has long been a significant challenge.

For convergence analysis, the frequency response curve for the Zone 1 is shown in Fig. 4. The analysis has been examined using both one and two mode expansions in the Galerkin decomposition method. As shown in Fig. 4, there is reasonable convergence for one mode. Therefore, it is sufficient to truncate the expansion series beyond the first mode.

Fig. 5, illustrate the frequency response curves for the Zone 1, with four different levels of V_{DC}.

As depicted in Fig. 5, when $V_{DC} = 50$V, the response exhibits several peaks in the super-harmonic regime. The dominant peak corresponds to the super-harmonic of order 1/2, while the preceding peak is associated with the super-harmonic of order 1/3. As V_{DC} increases from 50 V to 90 V, the softening effect induced by the applied electrostatic voltage leads to an increase in the amplification factor, which is the ratio of the peak dynamic displacement to the static deflection. Consequently, the two super-harmonic peaks merge, resulting in a broader super-harmonic resonance zone that combines the effects of the 1/2 and 1/3 order super-harmonics.

Fig. 6 illustrates similar results as Fig. 5 but with different AC voltage $V_{AC} = 100$V.

Comparing Fig. (6) with the relevant results in Fig. (5) reveals that the resonance zone is mainly affected by the value of the DC voltage rather than the AC voltage and the fact that the DC voltage whether lowers or higher the natural frequency depends on where we are on Fig. 2. However it can be concluded that increasing the level of the AC voltage dominates the nonlinearity and it activates the higher order super-harmonic resonances of orders 1/4, 1/5 and so on; this can be concluded from Fig. 6(d) as the higher orders of the super-harmonics have been closely located on the frequency response curve and as a result they have been collided and generated a wide band of resonance region. This is important particularly in case of wide band low frequency energy harvesters and also wide band MEMs band pass filters.

As illustrated in Fig. 7(a), when the system is excited at a frequency of $\Omega \approx \frac{1}{2}\omega_0 = 25.5$, the frequency spectrum of the response not only contains the excitation frequency (X), but also its integer multiples, namely 2X, 3X, and 4X. The presence of these higher harmonics facilitates the activation of super-harmonic resonances, which indirectly excite the system's primary resonance. In general, when the excitation

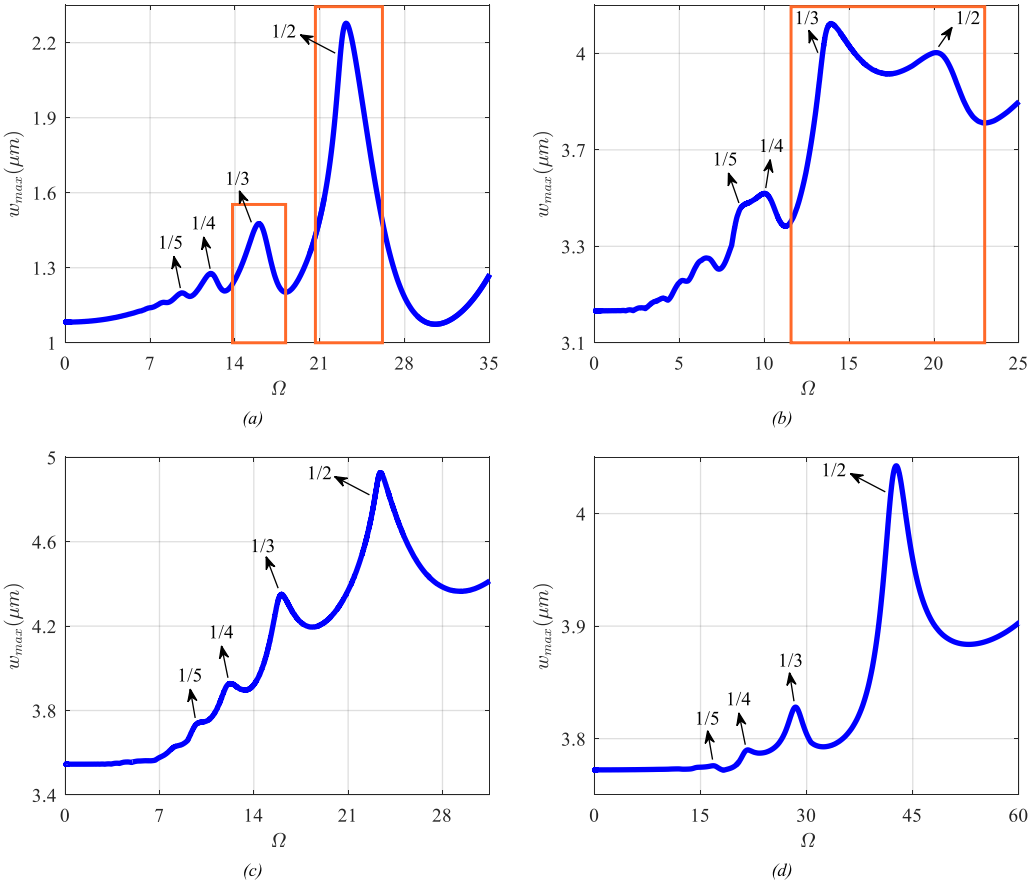

Fig. 5. Frequency response curve near super-harmonic secondary resonance for $V_p = 0$V, $V_{AC} = 30$V, $\xi = 0.06$ (a): $V_{DC} = 50$V, *(b)*: $V_{DC} = 90$V, *(c)*: $V_{DC} = 120$V, *(d)*: $V_{DC} = 180$V

frequency satisfies $\approx \frac{1}{n}\omega_0$, the resulting frequency multiplication generates integer multiples of $\frac{1}{n}\omega_0$. Among these, the nth harmonic can fall within the primary resonance range, thereby indirectly triggering the primary resonance. This mechanism is significant because it enables resonance to occur even under low-frequency excitation, which is particularly advantageous for low-frequency energy harvesters, where ambient mechanical vibrations are typically confined to lower frequency bands. The influence of the AC voltage amplitude on the system response has been investigated. Fig. 8 presents the frequency response curves in the super-harmonic regime for $V_{DC} = 50$V, corresponding to two distinct amplitudes of the AC voltage.

As illustrated, for a given DC voltage, as the AC voltage increases, the amplitude of the steady state response does also increase. The increase of the amplitude on the frequency response curves, leads in the appearance of further bifurcations including cyclic fold (CF) and Period doubling bifurcation points (PD). Although the amplitude of the current model is not constrained by the physical gap between the electrodes as is typically the case in parallel-plate capacitors (Ghavami et al., 2018, 2022) and thus the system is not subject to the conventional pull-in instability, the response becomes unstable at higher AC voltages. This instability is indicated by the dashed lines in Fig. 8, which represent mathematically unstable solution branches emerging from bifurcation points.

Fig. 9 illustrates the time response and the associated phase plane for $V_{DC} = 50$V, $V_{AC} = 50$V, $\Omega = 25$, which falls within the period doubled regio in Fig. 8 (a).

The effect of the variation of the damping ratio on the frequency response curves has been investigated in Fig. 10.

As the damping ratio decreases, the amplitude of the response increases, thereby amplifying the influence of nonlinear terms. This leads to the emergence of additional bifurcation points and the activation of higher-order super-harmonic resonances.

The effect of exciting piezoelectric layers with DC excitation, with different polarities has been investigated in Fig. 11.

By applying $V_p = +0.3V$, a tensile axial force is applied to the microbeam in the longitudinal direction, leading to an increase in the linear stiffness and natural frequency of the system. Therefore, the frequency response curve shifts to the right in the frequency domain. As illustrated, applying $V_p = +0.3V$, not only shifts the frequency response curve rightward in the frequency domain but also reduces the amplitude of the steady-state response, indicating the dominance of linear terms. In contrast, By applying $V_p = -0.3V$, a compressive axial force is applied to the microbeam in the longitudinal direction, leading to a decrease in the linear stiffness and natural frequency of the system. Therefore, the frequency response curve shifts to the left in the frequency domain. Also, applying $V_p = -0.3V$ increases the response amplitude, thereby enhancing the influence of nonlinear terms and leading to the excitation of higher-order super-harmonics. This implies that piezoelectric excitation can serve not only as a resonance frequency tuning mechanism (Azizi et al., 2014), but also as a bandwidth tuning tool an interesting and promising characteristic, given that bandwidth tunability is of critical importance in the design of MEMS sensors and actuators.

Fig. 12 illustrates the force response curves for $V_p = 0$V, $V_{DC} = 50$V, and two different excitation frequencies, $\Omega = 20$ and $\Omega = 25$. The primary resonance frequency, ω_0, corresponding to the applied DC voltage, is (Azizi et al., 2014). This results in the super-harmonic resonance of order 1/2, occurring approximately at [25.5] and accordingly the system exhibits higher amplitudes in Fig. 12(a), in the vicinity of the super-harmonic resonance of order 1/2. These higher amplitudes are

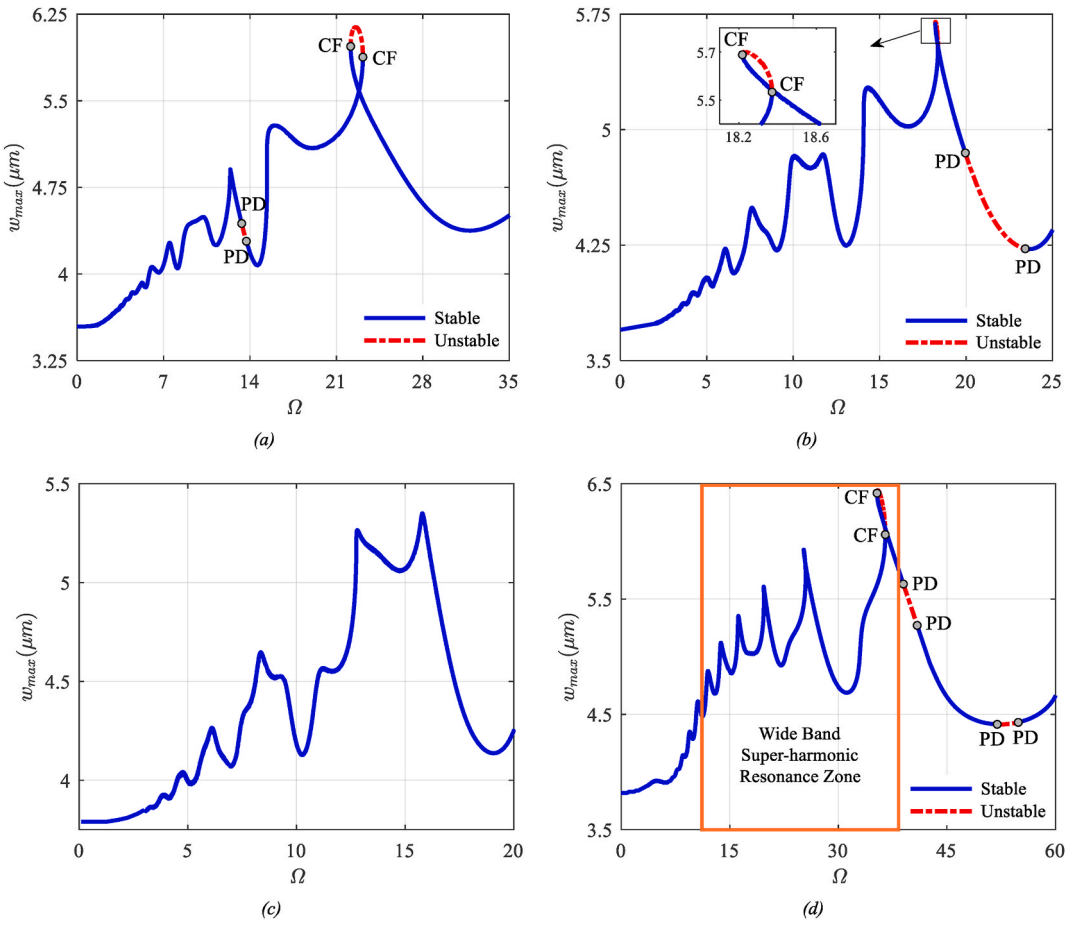

Fig. 6. Frequency response curve near super-harmonic resonance for $V_p = 0$V, $V_{AC} = 100$V, $\xi = 0.06$ (a): $V_{DC} = 50$V, *(b)*: $V_{DC} = 90$V, *(c)*: $V_{DC} = 120$V, *(d)*: $V_{DC} = 180$V

associated with two period-doubling bifurcations in Fig. 12(b). The presence of these bifurcations suggests that the system has the potential to exhibit even more complex dynamics, potentially transitioning to chaotic behavior through a cascade of period-doubling bifurcations.

4. Conclusion

The nonlinear dynamics of an initially curved microbeam, sandwiched between two piezoelectric layers and subjected to fringing-field electrostatic actuation, were investigated. The displacement-dependent nature of the electrostatic force was analysed using a finite element-based approach implemented in COMSOL. The equation of motion was derived and reduced to a finite-degree-of-freedom model using the Galerkin-based method. The effects of both DC and AC electrostatic voltages on the system's response were studied. It was found that, unlike traditional parallel-plate capacitors where electrostatic excitation typically introduces a softening effect and limits amplitude due to pull-in instability, the fringing-field electrostatic excitation does not impose such limitations. Instead, it can either increase or decrease the natural frequency, depending on the applied level of DC voltage. Additionally, increasing the AC voltage for a given DC level enhances the influence of nonlinear terms, thereby activating higher-order super-harmonic resonances. Super-harmonics of order 1/2 and 1/3 were observed even at relatively low AC voltages, while higher orders (e.g., 1/4 and 1/5) were activated as the AC voltage increased. The absence of pull-in instability allows the microbeam to undergo large-amplitude vibrations, enabling the generation of multiple, closely spaced super-harmonic resonances. These overlapping resonances result in the formation of a wide-band super-harmonic resonance zone. This behaviour is particularly valuable for the development of low-frequency, wide-band MEMS energy harvesters, as ambient mechanical vibrations typically occur in the lower frequency ranges. Similarly, it holds promise for the design of wide-band MEMS band-pass filters an area where achieving a broad bandwidth remains a significant challenge. The effect of the DC voltage on the piezoelectric layers was also examined. It was observed that piezoelectric excitation can function not only as a mechanism for tuning resonance frequency but also as a tool for adjusting bandwidth an intriguing and promising feature, given that bandwidth tunability is crucial in the design of MEMS sensors and actuators. Furthermore, increasing the AC voltage was found to generate additional bifurcation points in the frequency response curves, including cyclic fold and period-doubling bifurcations. The findings of this study are promising for the future design and fabrication of MEMS wide-band energy harvesters and band-pass filters.

CRediT authorship contribution statement

Zahra Rashidi: Writing – original draft, Software, Investigation, Formal analysis. **Saber Azizi:** Writing – review & editing, Writing – original draft, Supervision, Methodology, Conceptualization. **Omid Rahmani:** Writing – review & editing.

Declaration of competing interest

The authors declare that they have no known competing financial interests or personal relationships that could have appeared to influence the work reported in this paper.

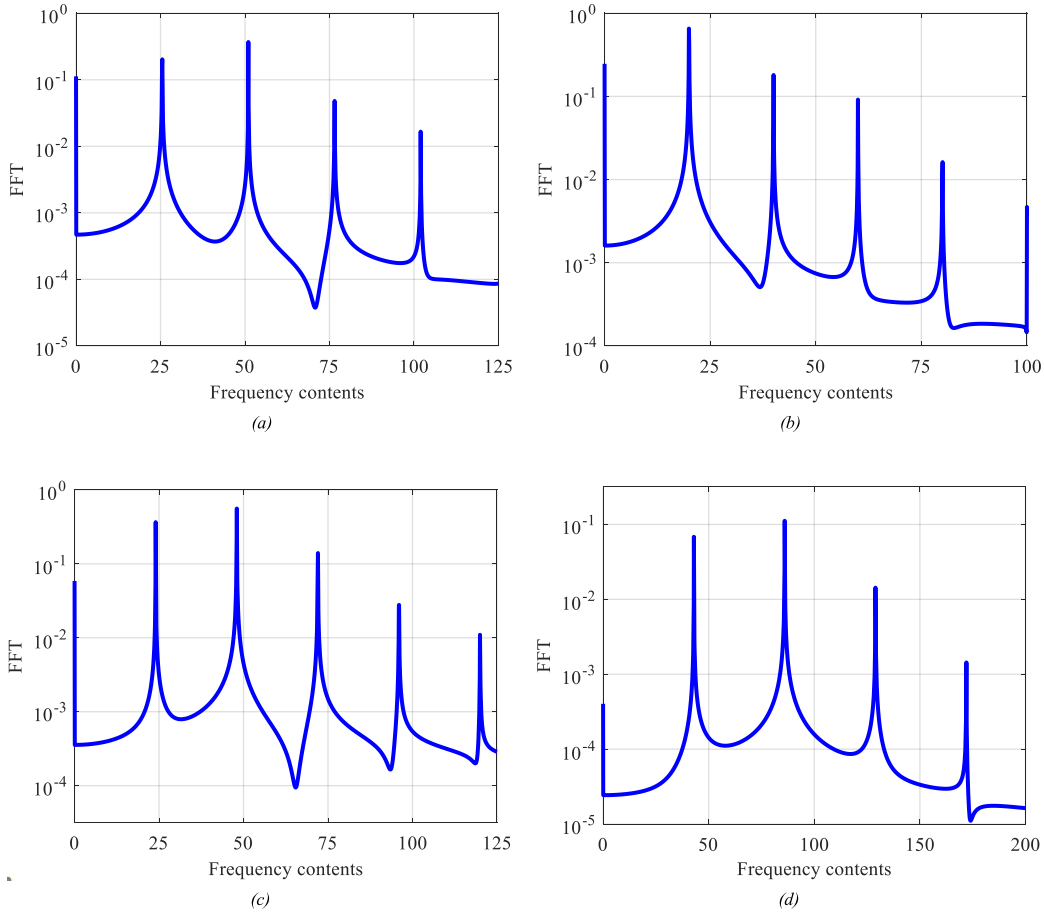

Fig. 7. Frequency spectrum for $\Omega \approx \frac{1}{2}\omega_0$, $V_p = 0$V, $V_{AC} = 30$V, $\xi = 0.06$ (a): $V_{DC} = 50$V, $\Omega = 25.5$, *(b)*: $V_{DC} = 90$V, $\Omega = 20$, *(c)*: $V_{DC} = 120$V, $\Omega = 24$, *(d)*: $V_{DC} = 180$V, $\Omega = 43$

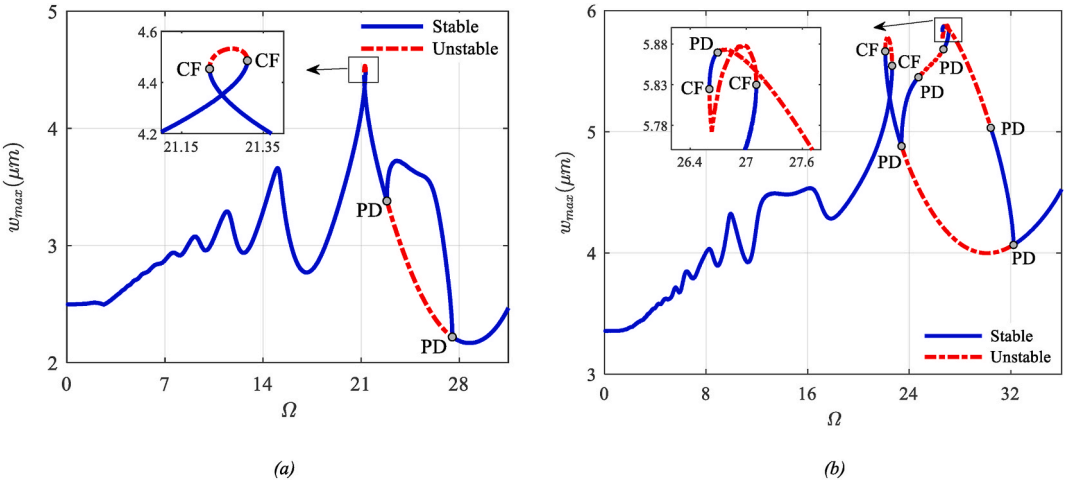

Fig. 8. Frequency response curve near super-harmonic resonance for $V_p = 0$V, $V_{DC} = 50$V, $\xi = 0.06$ *(a)*: $V_{AC} = 50$V, *(b)*: $V_{AC} = 80$V

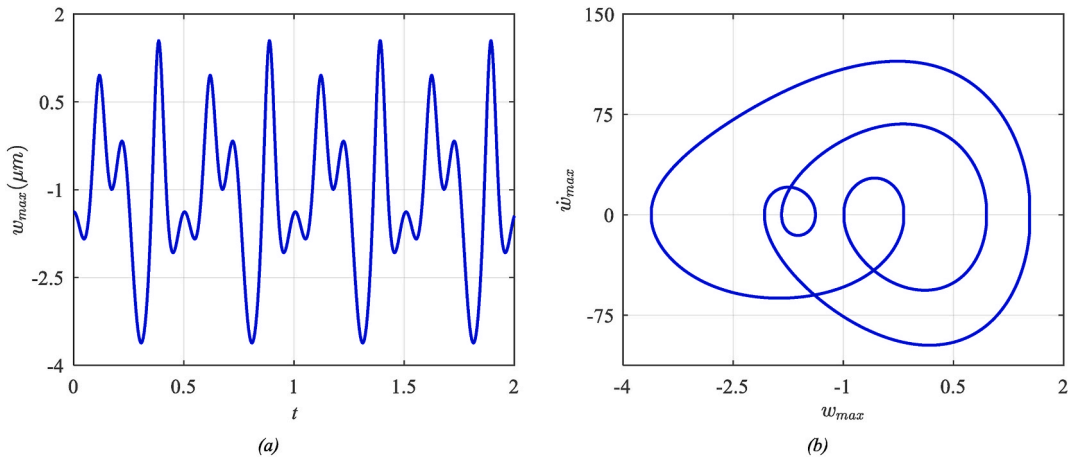

Fig. 9. Response for $V_p = 0$V, $V_{DC} = 50$V, $V_{AC} = 50$V, $\Omega = 25$ *(a):* Time response, *(b):* Phase plane.

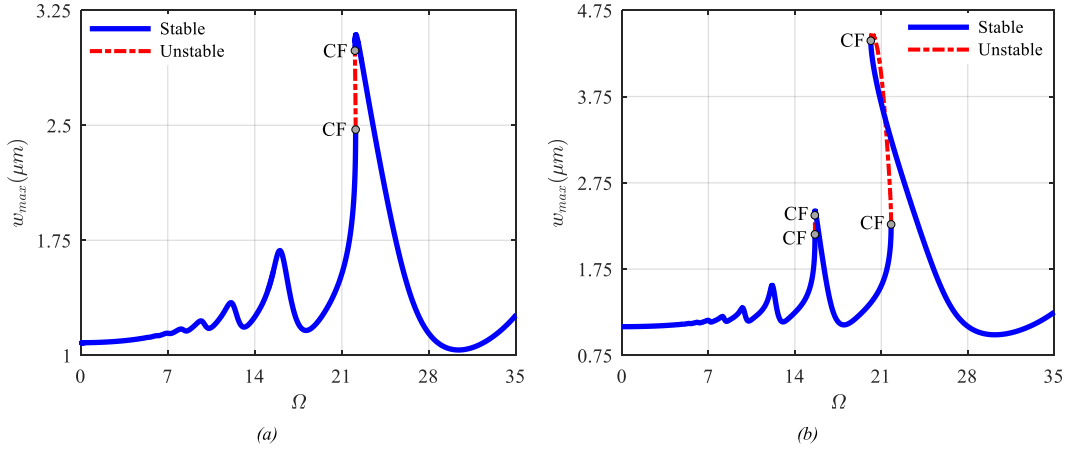

Fig. 10. Frequency response curve near super-harmonic resonance for $V_p = 0$V, $V_{DC} = 50$V, $V_{AC} = 30$V, *(a)*: $\xi = 0.04$, *(b)*: $\xi = 0.02$

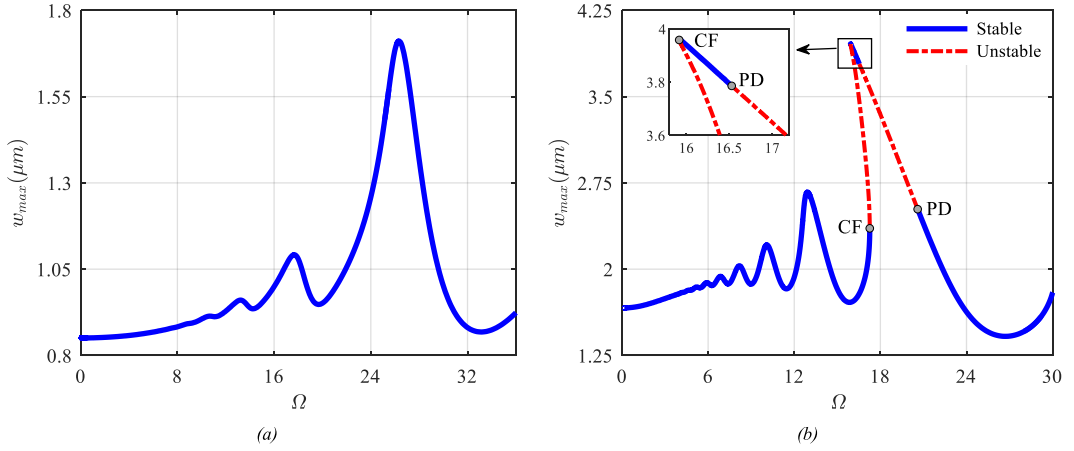

Fig. 11. Frequency response curve near super-harmonic resonance for $V_{DC} = 50$V, $V_{AC} = 30$V, $\xi = 0.06$, *(a):* $V_p = +0.3$V, *(b):* $V_p = -0.3$V

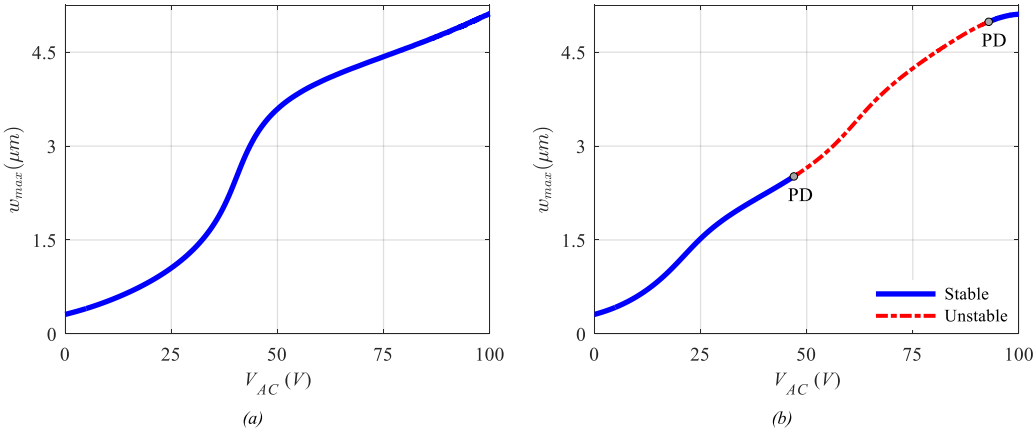

Fig. 12. Force response curves corresponding to *(a)*: $\Omega = 20$, *(b)*: $\Omega = 25$ *w ith* $V_p = 0\text{V}, V_{DC} = 50\text{V}, \xi = 0.06$

Appendix A

In this section, the normalized mode shapes of the straight microbeam $(\varphi_i(x))$, which can be used as the admissible functions in the Galerkin method, are presented. The equation governing the normalized mode shapes of the double-clamped straight microbeam, taking into account the effect of the axial force due to piezoelectric excitation, can be expressed as follows

$$\varphi_i^{(iv)} = P\varphi_i'' + \omega_i{}^2\varphi_i\varphi_i(0) = 0, \varphi_i(1) = 0, \varphi_i'(0) = 0, \varphi_i'(1) = 0 \tag{A1}$$

where, ω_i is the i-th natural frequency of the microbeam. By solving the above equation, the normalized mode shapes are determined as follows

$$\varphi_i(x) = A\left[sin\, s_1 x - \frac{s_1}{s_2} sinh\, s_2 x - \frac{sin\, s_1 - \frac{s_1}{s_2} sinh\, s_2}{cos\, s_1 - cosh\, s_2}(cos\, s_1 x - cosh\, s_2 x)\right] \tag{A2}$$

where

$$s_1 = \sqrt{\frac{\sqrt{P^2 + 4\omega_i{}^2} - P}{2}} i\, s_2 = \sqrt{\frac{\sqrt{P^2 + 4\omega_i{}^2} + P}{2}} \tag{A3}$$

Also, the value of A is obtained using the following orthogonality condition

$$\int_0^1 (\varphi_i)^2 dx = 1 \tag{A4}$$

Appendix B

This section provides information about shooting and continuation methods and stability analysis of periodic solutions.

The equations take the general form $\ddot{u}_n + F(u_n, \dot{u}_n, t) = 0$ and the shooting method ensures periodicity by satisfying $u_n(0) = u_n(T)$ and $\dot{u}_n(0) = \dot{u}_n(T)$, where T is the period. In fact, in this method, initial guesses are considered for the initial conditions. Then the initial guesses are corrected. Convergence is achieved when the difference between the new and previous corrected initial guesses is reduced to a very small value. The most important advantage of the shooting method is that integration is performed only over a single period. Therefore, the shooting method is a fast method for finding periodic solutions. The shooting method is a numerical method for obtaining both stable and unstable periodic solutions. However, depending on the studied model, finding unstable periodic solutions may require a lot of iterations or multiple initial guesses.

Continuation was applied to trace the response as the excitation frequency varied. Matcont is used as a continuation toolbox for ODEs. In general, numerical continuation methods are used to compute solution curves of the nonlinear equations of the form

$$F(x) = 0 \tag{B1}$$

where, $F : R^{n+1} \rightarrow R^n$ is a smooth function. Numerical continuation is a method for calculating successive sequences of points that approximate the desired branch. Most continuation algorithms implement a predictor-corrector scheme. The idea of this scheme is to generate a sequence of points x_i, $i = 1, 2, 3, \ldots$ along the curve that satisfy the tolerance criterion

$$\|F(x_i)\| \leq \epsilon, \epsilon > 0 \tag{B2}$$

Starting from an initial point on the continuation path, the goal is to trace the rest of the path in steps. At each step, the algorithm first predicts the next point on the continuation path along the tangent direction and then corrects the predicted point towards the solution curve. Matcont uses the so called Moore-Penrose corrections; this amounts to using a variant of Newton's method for the corrector step.

More details regarding the shooting and continuation methods have been provided in Refs. (Younis, 2011; Govaerts et al., 2019).

The stability analysis of periodic solutions can be performed by obtaining the eigenvalues of the monodromy matrix, so called Floquet multipliers. If the absolute value of all the eigenvalues is less than one, then the periodic solution will be stable. However, if at least one of the eigenvalues has a magnitude greater than one, the periodic solution will be unstable.

Data availability

No data was used for the research described in the article.

References

Azizi, S., Ghazavi, M.R., Rezazadeh, G., Ahmadian, I., Cetinkaya, C., 2014. Tuning the primary resonances of a micro resonator, using piezoelectric actuation. Nonlinear Dyn. 76 (1), 839–852. https://doi.org/10.1007/s11071-013-1173-4, 2014/04/01.

Azizi, S., Chorsi, M.T., Bakhtiari-Nejad, F., 2016. On the secondary resonance of a MEMS resonator: a conceptual study based on shooting and perturbation methods. Int. J. Non Lin. Mech. 82, 59–68. https://doi.org/10.1016/j.ijnonlinmec.2016.02.003, 2016/06/01.

Bell, D.J., Lu, T.J., Fleck, N.A., Spearing, S.M., 2005. MEMS actuators and sensors: observations on their performance and selection for purpose. J. Micromech. Microeng. 15 (7), S153. https://doi.org/10.1088/0960-1317/15/7/022, 2005/06/20.

Bogue, R., 2013. Recent developments in MEMS sensors: a review of applications, markets and technologies. Sens. Rev. 33 (4), 300–304. https://doi.org/10.1108/SR-05-2013-678.

A. Bouchaala et al., "Nonlinear-based MEMS sensors and active switches for gas detection," Sensors, vol. 16, no. 6, doi: 10.3390/s16060758.

Caruntu, D.I., Luo, L., 2014. Frequency response of primary resonance of electrostatically actuated CNT cantilevers. Nonlinear Dyn. 78 (3), 1827–1837. https://doi.org/10.1007/s11071-014-1537-4, 2014/11/01.

Caruntu, D.I., Martinez, I., 2014. Reduced order model of parametric resonance of electrostatically actuated MEMS cantilever resonators. Int. J. Non Lin. Mech. 66, 28–32. https://doi.org/10.1016/j.ijnonlinmec.2014.02.007, 2014/11/01/.

Charlot, B., Sun, W., Yamashita, K., Fujita, H., Toshiyoshi, H., 2008. Bistable nanowire for micromechanical memory. J. Micromech. Microeng. 18 (4), 045005. https://doi.org/10.1088/0960-1317/18/4/045005, 2008/02/22.

Dhooge, A., Govaerts, W., Kuznetsov, Y.A., 2003. MATCONT: a MATLAB package for numerical bifurcation analysis of ODEs. ACM Trans. Math. Softw. 29 (2), 141–164. https://doi.org/10.1145/779359.779362.

Eihab, M.A.-R., Ali, H.N., 2003. Secondary resonances of electrically actuated resonant microsensors. J. Micromech. Microeng. 13 (3), 491. https://doi.org/10.1088/0960-1317/13/3/320, 2003/04/15.

Ghavami, M., Azizi, S., Ghazavi, M.R., 2018. On the dynamics of a capacitive electret-based micro-cantilever for energy harvesting. Energy 153, 967–976. https://doi.org/10.1016/j.energy.2018.04.034, 2018/06/15.

Ghavami, M., Azizi, S., Ghazavi, M.R., 2022. Dynamics of a micro-cantilever for capacitive energy harvesting considering nonlinear inertia and curvature. J. Braz. Soc. Mech. Sci. Eng. 44 (4), 124. https://doi.org/10.1007/s40430-021-03301-0, 2022/03/10.

Ghayesh, M.H., Farokhi, H., 2017. Bistable nonlinear response of MEMS resonators. Nonlinear Dyn. 90 (3), 1627–1645. https://doi.org/10.1007/s11071-017-3753-1, 2017/11/01.

Ghayesh, M.H., Farokhi, H., Amabili, M., 2013. Nonlinear behaviour of electrically actuated MEMS resonators. Int. J. Eng. Sci. 71, 137–155. https://doi.org/10.1016/j.ijengsci.2013.05.006.

Ghayesh, M.H., Farokhi, H., Alici, G., 2015. Size-dependent electro-elasto-mechanics of MEMS with initially curved deformable electrodes. Int. J. Mech. Sci. 103, 247–264. https://doi.org/10.1016/j.ijmecsci.2015.09.011, 2015/11/01.

Govaerts, W., et al., 2019. MATCONT: Continuation Toolbox for Odes in Matlab, vol. 4, p. 2020. *Retrieved December*.

Gu, L., 2011. Low-frequency piezoelectric energy harvesting prototype suitable for the MEMS implementation. Microelectron. J. 42 (2), 277–282. https://doi.org/10.1016/j.mejo.2010.10.007, 2011/02/01.

Han, M., Yuan, Q., Sun, X., Zhang, H., 2014. Design and fabrication of integrated magnetic MEMS energy harvester for low frequency applications. J. Microelectromech. Syst. 23 (1), 204–212. https://doi.org/10.1109/JMEMS.2013.2267773.

Jaber, N., Ramini, A., Hennawi, Q., Younis, M.I., 2016. Wideband MEMS resonator using multifrequency excitation. Sensor Actuator Phys. 242, 140–145. https://doi.org/10.1016/j.sna.2016.02.030, 2016/05/01.

Kacem, N., Baguet, S., Hentz, S., Dufour, R., 2011. Computational and quasi-analytical models for non-linear vibrations of resonant MEMS and NEMS sensors. Int. J. Non Lin. Mech. 46 (3), 532–542. https://doi.org/10.1016/j.ijnonlinmec.2010.12.012, 2011/04/01.

Liu, H., Tay, C.J., Quan, C., Kobayashi, T., Lee, C., 2011. Piezoelectric MEMS energy harvester for low-frequency vibrations with wideband operation range and steadily increased output power. J. Microelectromech. Syst. 20 (5), 1131–1142. https://doi.org/10.1109/JMEMS.2011.2162488.

Mestrom, R.M.C., Fey, R.H.B., van Beek, J.T.M., Phan, K.L., Nijmeijer, H., 2008. Modelling the dynamics of a MEMS resonator: simulations and experiments. Sensor Actuator Phys. 142 (1), 306–315. https://doi.org/10.1016/j.sna.2007.04.025, 2008/03/10.

Michel, A.R., Dirk De, B., Armin, R.V., Eric, P., John, D., 2004. A novel external electrode configuration for the electrostatic actuation of MEMS based devices. J. Micromech. Microeng. 14 (4), 446. https://doi.org/10.1088/0960-1317/14/4/003, 2004/01/09.

Miller, L.M., Halvorsen, E., Dong, T., Wright, P.K., 2011. Modeling and experimental verification of low-frequency MEMS energy harvesting from ambient vibrations. J. Micromech. Microeng. 21 (4), 045029. https://doi.org/10.1088/0960-1317/21/4/045029, 2011/03/24.

Najar, F., Nayfeh, A.H., Abdel-Rahman, E.M., Choura, S., El-Borgi, S., 2010. Nonlinear analysis of MEMS electrostatic microactuators: primary and secondary resonances of the first mode. J. Vib. Control 16 (9), 1321–1349. https://doi.org/10.1177/1077546309106520, 2010/08/01.

Najar, F., Ghommem, M., Abdelkefi, A., 2020. A double-side electrically-actuated arch microbeam for pressure sensing applications. Int. J. Mech. Sci. 178, 105624. https://doi.org/10.1016/j.ijmecsci.2020.105624, 2020/07/15.

Nayfeh, A.H., Balachandran, B., 2008. Applied Nonlinear Dynamics: Analytical, Computational, and Experimental Methods. John Wiley & Sons.

Nayfeh, A.H., Younis, M.I., 2005. Dynamics of MEMS resonators under superharmonic and subharmonic excitations. J. Micromech. Microeng. 15 (10), 1840. https://doi.org/10.1088/0960-1317/15/10/008, 2005/08/09.

Nguyen, D.S., Halvorsen, E., Jensen, G.U., Vogl, A., 2010. Fabrication and characterization of a wideband MEMS energy harvester utilizing nonlinear springs. J. Micromech. Microeng. 20 (12), 125009. https://doi.org/10.1088/0960-1317/20/12/125009, 2010/11/09.

Nikpourian, A., Ghazavi, M.R., Azizi, S., 2019a. Size-dependent secondary resonance of a piezoelectrically laminated bistable MEMS arch resonator. Compos. B Eng. 173, 106850. https://doi.org/10.1016/j.compositesb.2019.05.061, 2019/09/15.

Nikpourian, A., Ghazavi, M.R., Azizi, S., 2019b. Size-dependent nonlinear behavior of a piezoelectrically actuated capacitive bistable microstructure. Int. J. Non Lin. Mech. 114, 49–61. https://doi.org/10.1016/j.ijnonlinmec.2019.04.010, 2019/08/01.

Nisanth, A., Suja, K.J., Seena, V., 2021. Design and optimization of MEMS piezoelectric energy harvester for low frequency applications. Microsyst. Technol. 27 (1), 251–261. https://doi.org/10.1007/s00542-020-04944-0, 2021/01/01.

Ouakad, H.M., 2013. An electrostatically actuated MEMS arch band-pass filter. Shock Vib. 20, 809–819. https://doi.org/10.3233/SAV-130786.

Ouakad, H.M., Younis, M.I., 2010. The dynamic behavior of MEMS arch resonators actuated electrically. Int. J. Non Lin. Mech. 45 (7), 704–713. https://doi.org/10.1016/j.ijnonlinmec.2010.04.005, 2010/09/01.

Pasharavesh, A., Ahmadian, M.T., 2017. Characterization of a nonlinear MEMS-Based piezoelectric resonator for wideband micro power generation. Appl. Math. Model. 41, 121–142. https://doi.org/10.1016/j.apm.2016.08.019, 2017/01/01.

Ramini, A.H., Hennawi, Q.M., Younis, M.I., 2016. Theoretical and experimental investigation of the nonlinear behavior of an electrostatically actuated In-Plane MEMS arch. J. Microelectromech. Syst. 25 (3), 570–578. https://doi.org/10.1109/JMEMS.2016.2554659.

Rashidi, Z., Azizi, S., Rahmani, O., 2023a. Nonlinear dynamics of a piezoelectrically laminated initially curved microbeam resonator exposed to fringing-field electrostatic actuation. Nonlinear Dyn. https://doi.org/10.1007/s11071-023-08915-8, 2023/10/14.

Rashidi, Z., Azizi, S., Rahmani, O., 2023b. Nonlinear dynamics of a piezoelectrically laminated initially curved microbeam resonator exposed to fringing-field electrostatic actuation. Nonlinear Dyn. 111 (22), 20715–20733. https://doi.org/10.1007/s11071-023-08915-8, 2023/11/01.

Rashidi, Z., Azizi, S., Rahmani, O., 2024. Period-doubling Cascade route to chaos in an initially curved microbeam resonator exposed to fringing-field electrostatic actuation. Nonlinear Dyn. 112 (12), 9915–9932. https://doi.org/10.1007/s11071-024-09575-y, 2024/06/01.

Rebeiz, G.M., Muldavin, J.B., 2001. RF MEMS switches and switch circuits. IEEE Microw. Mag. 2 (4), 59–71. https://doi.org/10.1109/6668.969936.

Roundy, S., Wright, P.K., Rabaey, J., 2003. A study of low level vibrations as a power source for wireless sensor nodes. Comput. Commun. 26 (11), 1131–1144. https://doi.org/10.1016/S0140-3664(02)00248-7, 2003/07/01.

Ruzziconi, L., Bataineh, A.M., Younis, M.I., Cui, W., Lenci, S., 2013. Nonlinear dynamics of an electrically actuated imperfect microbeam resonator: experimental investigation and reduced-order modeling. J. Micromech. Microeng. 23 (7), 075012. https://doi.org/10.1088/0960-1317/23/7/075012, 2013/06/10.

Ruzziconi, L., Jaber, N., Kosuru, L., Bellaredj, M.L., Younis, M.I., 2021. Internal resonance in the higher-order modes of a MEMS beam: experiments and global analysis. Nonlinear Dyn. 103 (3), 2197–2226. https://doi.org/10.1007/s11071-021-06273-x, 2021/02/01.

Shim, Y., Wu, Z., Rais-Zadeh, M., 2012. A high-performance continuously tunable MEMS bandpass filter at 1 GHz. IEEE Trans. Microw. Theor. Tech. 60 (8), 2439–2447. https://doi.org/10.1109/TMTT.2012.2198228.

Tajaddodianfar, F., Nejat Pishkenari, H., Hairi Yazdi, M.R., Maani Miandoab, E., 2015. On the dynamics of bistable micro/nano resonators: analytical solution and nonlinear behavior. Communications in Nonlinear Science and Numerical

Simulation 20 (3), 1078–1089. https://doi.org/10.1016/j.cnsns.2014.06.048, 2015/03/01.
Tajaddodianfar, F., Yazdi, M.R.H., Pishkenari, H.N., 2017. Nonlinear dynamics of MEMS/NEMS resonators: analytical solution by the homotopy analysis method. Microsyst. Technol. 23 (6), 1913–1926. https://doi.org/10.1007/s00542-016-2947-7, 2017/06/01.
Tausiff, M., Ouakad, H.M., Alqahtani, H., Alofi, A., 2019. Local nonlinear dynamics of MEMS arches actuated by fringing-field electrostatic actuation. Nonlinear Dyn. 95 (4), 2907–2921. https://doi.org/10.1007/s11071-018-4731-y, 2019/03/01.
Williams, C.B., Yates, R.B., 1996. Analysis of a micro-electric generator for microsystems. Sensor Actuator Phys. 52 (1), 8–11. https://doi.org/10.1016/0924-4247(96)80118-X, 1996/03/01.
Younesian, D., Sadri, M., Esmailzadeh, E., 2014. Primary and secondary resonance analyses of clamped–clamped micro-beams. Nonlinear Dyn. 76 (4), 1867–1884. https://doi.org/10.1007/s11071-014-1254-z, 2014/06/01.
Younis, M.I., 2011. MEMS Linear and Nonlinear Statics and Dynamics. Springer Science & Business Media.
Younis, M.I., Nayfeh, A.H., 2003. A study of the nonlinear response of a resonant microbeam to an electric actuation. Nonlinear Dyn. 31 (1), 91–117. https://doi.org/10.1023/A:1022103118330, 2003/01/01.
Younis, M.I., Ouakad, H.M., Alsaleem, F.M., Miles, R., Cui, W., 2010. Nonlinear dynamics of MEMS arches under harmonic electrostatic actuation. J. Microelectromech. Syst. 19 (3), 647–656. https://doi.org/10.1109/JMEMS.2010.2046624.